


Article

Multi-Parameter Optimization of an InP Electro-Optic Modulator

Mikhail Stepanenko, Igor Yunusov *, Vadim Arykov, Pavel Troyan and Yury Zhidik 

Integrated Optics and Microwave Photonics Laboratory, Tomsk State University of Control Systems and Radioelectronics, 634050 Tomsk, Russia; stepanenko.m@ir-mw.com (M.S.); arykov.v@ir-mw.com (V.A.); tpe@tusur.ru (P.T.); zhidikyur@mail.ru (Y.Z.)

* Correspondence: yunusov.i@ir-mw.com

Received: 19 October 2020; Accepted: 18 November 2020; Published: 21 November 2020



Abstract: In this article, a method for indium phosphide (InP) electro-optic modulator (EOM) optimization is introduced. The method can be used for the design and analysis of an EOM based on the Mach-Zehnder interferometer (MZI) design. This design is based on the division of the input optical signal into two optical paths and then, after processing, it combines the light into a single waveguide. The symmetry of the structure can provide state-of-the-art EOM characteristics with a push-pull control signal. Using a traveling wave electrode (TWE) design as a starting point, the authors varied the heterostructure design and optical waveguide parameters to obtain the optimal values of initial optical loss, evenness of the initial optical loss in the operating wavelength range, and the extinction ratio and length of the modulator arm. The key features of the proposed optimization method include the following: all independent input parameters are linked into a single system, where the relationship between the electrical and optical parameters of the modulator is realized; all physically realizable combinations of the input parameters are available for analysis; and EOM optimization is possible for one target parameter or for a group of target parameters. The results of the EOM optimization using the described method are presented.

Keywords: multi-quantum well; traveling wave electrodes; electro-optic modulator; indium phosphide

1. Introduction

Electro-optic modulators (EOMs) are widely used for the phase or intensity modulation of light waves in digital and analog fiber-optic systems. High-speed modulators are of particular interest due to their practical application in advanced telecommunication systems, radio-over-fiber systems, and test and measurement equipment [1–3]. For the purpose of high-speed modulation, lithium niobate [4], organic materials [5], and compound semiconductor systems [6] are used. Modulators based on compound semiconductor systems are preferable to the other types of modulators due to their small size and the possibility of integrating them with other active and passive optical elements on a single chip (lasers, semiconductor optical amplifiers, couplers and dividers, arrayed waveguide gratings, photodetectors, etc.) [7].

Modulators based on compound semiconductor systems can control light wave propagation using two physical effects: change in permittivity (EOM) [8] or change in the light absorption coefficient (electro-absorption modulators (EAMs) [9] in optical waveguide media under the conditions of an applied alternating electric field.

Although EAMs are compact devices, their use is limited to intensity modulation. Moreover, EAMs demonstrate a relatively poor extinction ratio and a relatively narrow optical signal operating wavelength range. EOMs may be preferable due to their all-purpose nature: both the phase and the intensity can be controlled effectively. Additionally, EOMs exhibit a high extinction ratio and a

relatively broad optical bandwidth. For the intensity control, a Mach-Zehnder interferometer (MZI) design [10] is used. Furthermore, EOMs use the push-pull principle [11] and have symmetrical electrodes and optical arm topology.

The symmetry of MZI arms is one of the most important concepts used in MZI EOM implementation. This feature provides the equality of signal phases in the outputs of arms when no control signal is applied; thus, minimal signal loss occurs in the “open” state of an EOM. In the same manner, the symmetry of the arms can provide approximately equal signal intensities in the outputs of the EOM arms. This is particularly important when obtaining minimal output power in the “closed” state of an EOM, when the optical signals from the arms interfere with the π phase difference. In addition, the symmetrical layout of the device affords the opportunity to use the push-pull principle easily, i.e., to control light in both arms simultaneously using electrical control signals with opposite phases. This can double the efficiency of the electro-optic (EO) conversion per length unit.

In this work, we discuss a high-speed indium phosphide (InP) EOM with an MZI design suitable for both analog and digital modulation of light with a wavelength of 1.55 μm . The specified EOM is a complex device that requires careful design; therefore, it is necessary to take into account and to optimize many input parameters to create an EOM with the following state-of-the-art target parameters: low initial optical loss, high extinction ratio, wide EO bandwidth, broad range of optical carrier signals, and low control signal amplitude.

EOM design practice shows that it is impossible to satisfy all of the requirements of all of the target parameters simultaneously, because the variation of some input parameters can influence different target parameters in opposite ways. Under such conditions, an important task is to find an EOM design method that possesses powerful capabilities for optimizing EOMs in terms of each target parameter.

Another key point is how the general approach to the design of EOMs is implemented. As a rule, optimization of the optical part (heterostructure design and optical waveguide parameters) and the electrical part (control electrodes) is performed separately, followed by synthesis of the obtained results [12]. In this paper, the authors propose an approach based on the primacy of control electrode design: characteristic impedance, effective refraction index, specific capacitance of the control electrodes, electrical signal loss, and period of internal electrodes. The optimized electrode parameters, as well as other input parameters (such as the molar composition and quantity of multi-quantum well (MQW) layers, the thickness of the heterostructure layers, the optical waveguide width, control and bias voltages, and the fill factor of the internal electrodes), are used to further calculate all target EOM parameters (e.g., minimal optical loss, unevenness of optical loss in the operating wavelength range, extinction ratio, and length of the EOM arms).

The method assumes calculation of the target parameter values for all combinations of the input parameters. The algorithm is implemented in such a way that all input parameters are mutually agreed and the results of the calculation correspond to physically possible objects. The obtained data are filtered in accordance with the requirements for the target parameter values. Then, the proposed multi-parameter data representation is used to perform convenient analysis, which provides a set of appropriate combinations of the input parameters and allows highlighting the input parameters that are the most critical for the device’s performance. In the last step, the EOM can be optimized by choosing the critical input parameter values to satisfy the requirements of the particular target parameters.

The main aim of the work was to describe the proposed method and to show an example of its use for the optimization of an EOM with a 1530–1560 nm operating wavelength range.

2. Theory

In this section, we discuss the principles and key design points that are important for EOM functioning. The calculation algorithm introduced further in Section 3 is based on the main relationships of the electrodes and optical waveguide, which are described in the subsections below.

2.1. EOM Electrode Design

In this work, we considered the optimization of an EOM by exploiting the traveling wave electrode (TWE) design and the push-pull principle. The traveling wave concept was used to increase the efficiency of the interaction between the electrical and optical waves. The TWE of the EOM includes external and internal electrodes, as shown in Figure 1 [12]. The internal electrodes are represented by a set of periodic coplanar strip segments, which are electrically connected to the external electrodes. From an electrical point of view, the internal electrode segments perform as a periodic capacitive load for the line represented by the external electrodes. Two main requirements should be satisfied for the TWE. First, the TWE line should be designed around an impedance of 50 ohm to match commercial radio frequency drivers. Second, close alignment of the optical and electrical wave velocities is required to obtain the best interaction efficiency and to expand the bandwidth of the EO conversion. The latter means that the optical and microwave refractive indices should be equal for an ideal case (1).

$$n_{opt\ eff} = n_{\mu\ eff}, \quad (1)$$

where $n_{opt\ eff}$ is the optical effective refractive index, and $n_{\mu\ eff}$ is the microwave effective refractive index.

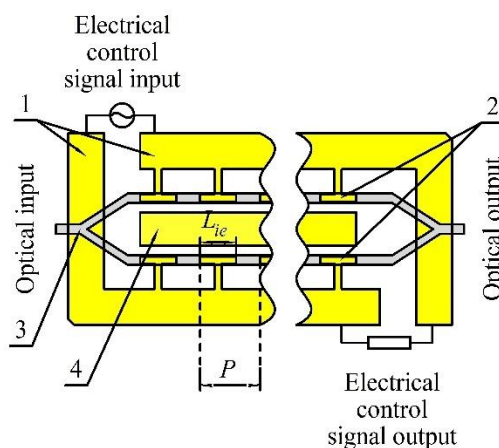


Figure 1. The scheme of the push-pull electro-optic modulator (EOM) with a traveling wave electrode (TWE) [12]: (1) external electrodes; (2) internal electrodes; (3) optical waveguide; and (4) bias control electrode.

In practice, the $n_{opt\ eff}$ value cannot be changed for a chosen waveguide material, and condition (1) can be obtained only by $n_{\mu\ eff}$ adjustment. The possibility of $n_{\mu\ eff}$ can be provided by the use of a TWE with segmented internal electrodes. The TWE with segmented internal electrodes provides the possibility of electrical signal phase velocity control.

The basic properties of the TWE must satisfy Equations (2) and (3) simultaneously to fit the requirements mentioned above.

$$Z_0 = (L_{\mu}/C_{\mu})^{1/2}, \quad (2)$$

where Z_0 is the transmission line characteristic impedance, L_{μ} is the specific inductance of the transmission line, and C_{μ} is the specific capacitance of the transmission line.

$$n_{\mu\ eff} = c(L_{\mu}C_{\mu})^{1/2}, \quad (3)$$

where c is the speed of light in the vacuum.

For a particular $n_{\mu\ eff}$, only one pair of values (L_{μ} and C_{μ}) that satisfies (2) and (3) exists. In the EOM, $n_{\mu\ eff}$ is tuned to match $n_{opt\ eff}$ by changing L_{μ} and C_{μ} .

The specific capacitance C_μ of the EOM TWE represents the sum of three components associated with the capacitance of the external electrodes, internal electrodes, and PIN diode waveguide structure (4) (see Figure 2). It is assumed in Equation (4) that PIN diode waveguide structures are connected in series with respect to the input control signal.

$$C_\mu = C_{\mu \text{ ext}} + C_{\mu \text{ int}} + \frac{C_{\mu \text{ pin}}}{2}, \quad (4)$$

where $C_{\mu \text{ ext}}$ is the specific capacitance of the external electrodes, $C_{\mu \text{ int}}$ is the specific capacitance of the internal electrodes, and $C_{\mu \text{ pin}}$ is the specific capacitance of the optical PIN diode waveguide structure.

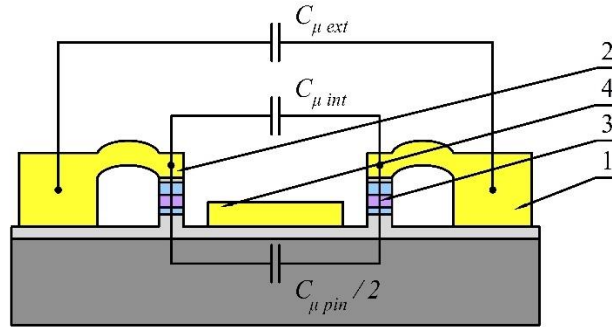


Figure 2. Schematic cross-section of EOM TWE: (1) external electrode; (2) internal electrode; (3) optical waveguide; and (4) bias control electrode.

The value of $C_{\mu \text{ pin}}$ is defined by the electrical fill factor of the internal electrodes, optical waveguide width, and heterostructure design. The electrical fill factor FF accounts for the fact that only a portion of the optical waveguide is covered by internal electrodes. The heterostructure design considered in this work corresponds to the layer stack presented in Figure 3. It consists of contact n^+ and p^+ InP layers, MQW layers, and p -spacer and n -spacer InP layers. The MQW stack consists of InGaAsP quantum well layers and InP barrier layers. The quantum well layer and barrier layer pair forms one MQW period. Since all layers between the contact n^+ and p^+ layers are undoped, the specific capacitance $C_{\mu \text{ pin}}$ can be expressed as shown in (5).

$$C_{\mu \text{ pin}} = FF [C_{diN}^{-1} + C_{diP}^{-1} + C_{MQW}^{-1}]^{-1}, \quad (5)$$

where C_{diN} is the specific capacitance of n -spacer, see (6); C_{diP} is the specific capacitance of p -spacer, see (7); C_{MQW} is the specific capacitance of MQW, see (8); and FF is the electrical fill factor, see (10).

$$C_{diN} = \frac{n_{InP}^2 \epsilon_0 W}{d_{iN}}, \quad (6)$$

where n_{InP} is the InP refractive index, ϵ_0 is the vacuum permittivity, W is the optical waveguide width, and d_{iN} is the n -spacer thickness.

$$C_{diP} = \frac{n_{InP}^2 \epsilon_0 W}{d_{iP}}, \quad (7)$$

where d_{iP} is the p -spacer thickness.

$$C_{MQW} = \frac{n_{MQW \text{ eff}}^2 \epsilon_0 W}{N(d_Q + d_B)}, \quad (8)$$

where $n_{MQW\ eff}$ is the effective MQW refractive index, see (9); N is the quantity of MQW periods; d_Q is the quantum well thickness; and d_B is the barrier layer thickness.

$$n_{MQW\ eff} = \frac{d_B \cdot n_{InP} + d_Q \cdot n_{InGaAsP}}{d_B + d_Q}, \quad (9)$$

where $n_{InGaAsP}$ is the InGaAsP refractive index (depending on the molar composition in the quantum well layer; see Section 2.2.2).

$$FF = L_{ie}/P, \quad (10)$$

where L_{ie} is the length of the internal electrodes (see Figure 1), and P is the period of the internal electrodes (see Figure 1).

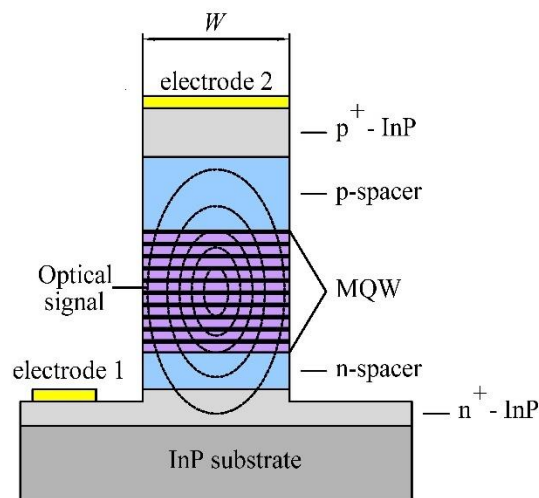


Figure 3. Schematic cross-section of the PIN diode waveguide structure.

The specific capacitance of the PIN diode waveguide structure $C_{\mu\ pin}$ introduced in this subsection is an important parameter for the performance of the EOM. The value of $C_{\mu\ pin}$ is connected to the electric field strength in the PIN diode waveguide structure. Under the conditions when all design parameters and the control voltage are kept constant, a higher $C_{\mu\ pin}$ corresponds to a higher electric field. Hence, higher $C_{\mu\ pin}$ values allow using the non-linear optical properties of waveguide media more intensely and provide higher EO conversion efficiency.

As can be seen from (4), a higher $C_{\mu\ pin}$ can be obtained only by a reduction in $C_{\mu\ ext}$, because C_{μ} must stay constant and $C_{\mu\ int}$ is very hard to reduce. A few methods have been offered to obtain low $C_{\mu\ ext}$ values [8].

The calculation algorithm, considered further in Section 3, is based on the primacy of the $C_{\mu\ pin}$ value. This means that all of the parameters that are relevant to the EOM design (i.e., electrical fill factor, heterostructure layer parameters, and waveguide width) are calculated in such a way that the constancy of $C_{\mu\ pin}$ is provided.

2.2. Light Wave Propagation in the Optical Waveguide

In this subsection, we consider the main relationships associated with the physical effects that are both exploited for light wave control and responsible for optical loss occurrence.

Since the media of propagation are not homogeneous, the effects mentioned above should be calculated separately for each layer in the heterostructure stack. The optical fill factor concept is used to perform such calculations.

2.2.1. Waveguide Optical Fill Factor

Light propagates into the optical waveguide in several layers simultaneously. The intensity of the light spreads unevenly in the waveguide cross-section, and in each layer, the power density is different. In addition, each layer has its own optical properties (i.e., refractive index and absorption coefficient). The effect of a particular layer j on light propagation is taken into account by calculating the optical fill factor $\Gamma_{opt, j}$. For an arbitrary layer, $\Gamma_{opt, j}$ can be expressed as (11).

$$\Gamma_{opt, j} = \int_{u_j}^{u_{j+1}} du \int_0^W I_1(u) I_2(v) dv, \quad (11)$$

where $I_1(u)$ is the law of light intensity distribution in the waveguide along its height, see (12); and $I_2(v)$ is the law of light intensity distribution in the waveguide along its width, see (15).

$$I_1(u) = \frac{2}{d_{WG\ eff}} e^{\frac{-4\pi u^2}{d_{WG\ eff}^2}}, \quad (12)$$

where $d_{WG\ eff}$ is the effective waveguide thickness, see (13) [13].

$$d_{WG\ eff} = d_{MQW} + \frac{2}{k_0 \sqrt{n_{MQW\ eff}^2 \cos^2 \theta_m - n_{InP}^2}}, \quad (13)$$

where k_0 is the wave vector in the vacuum, and θ_m is the optical mode propagation angle.

The value of θ_m is calculated based on condition (14) assuming $m = 0$.

$$n_{MQW\ eff} \cdot k_0 \cdot \sin(\theta_m) \cdot d_{MQW} - 2 \operatorname{atan} \left(\frac{\sqrt{n_{MQW\ eff}^2 \cdot \cos^2(\theta_m)^2 - n_{InP}^2}}{n_{MQW\ eff} \cdot \sin(\theta_m)} \right) = \pi m. \quad (14)$$

$$I_2(v) = \frac{2}{W} \cdot e^{\frac{-4\pi v^2}{W^2}}. \quad (15)$$

The calculation of the optical fill factor is performed for all layers of the heterostructure stack, including the n^+ and p^+ contact layers. The values obtained for all of the layers are used to further calculate the total refractive index change and the total optical loss for a given EOM arm length.

2.2.2. Refractive Index Control

The main mechanism providing the operation of the EOM is a change in the effective refractive index of the composite waveguide media, which is induced by the alternating electric field strength. The main aim of refractive index control is to change the light wave phase velocity and, finally, the difference between the output and input light wave phases of the EOM arm. In this subsection, we consider the relationships that describe how the intensity of light is controlled in the MZI EOM.

Several EO effects are exploited to obtain refractive index control in the EOM. The model of refractive index change Δn_{WG} can be expressed as (16).

$$\Delta n_{WG} = \Delta n_P + \Delta n_K + \Delta n_{pl} + \Delta n_{bg} + \Delta n_{bf}, \quad (16)$$

where Δn_P is the change in the refractive index due to the linear EO effect (Pockels effect) [14], see (17); Δn_K is the change in the refractive index due to the quadratic EO effect (Kerr effect) [15], see (18); Δn_{pl} is the change in the refractive index due to intraband absorption by free charge carriers [8,15];

Δn_{bg} is the change in the refractive index due to band gap reduction [8,15]; and Δn_{bf} is the change in the refractive index due to conduction and valence band filling [8,15].

$$\Delta n_p = \frac{1}{2}n^3r_{41}E, \quad (17)$$

where n is the media refractive index, E is the electric field strength, and r_{41} is the tensor element defined using the Adachi model depending on the band gap energy of the semiconductor material and photon energy.

$$\Delta n_K = \frac{1}{2}n^3s_{12}E^2, \quad (18)$$

where n is the media refractive index, E is the electric field strength, and s_{12} is the tensor element depending on the band gap energy of the semiconductor material and photon energy.

The components associated with intraband absorption by free charge carriers Δn_{pl} and band gap reduction Δn_{bg} are sufficient for a high electron concentration ($>5 \times 10^{16} \text{ cm}^{-3}$). Since the EOM optical waveguide media are depleted of free charge carriers, Δn_{pl} and Δn_{bg} are not taken into account in the calculations. The component associated with conduction and valence band filling Δn_{bf} also takes a small effect relative to Δn_p and Δn_K , because the condition of the close proximity of the photon and band gap energies is not satisfied in the EOM.

The tensor elements r_{41} and s_{12} associated with the linear and quadratic electro-optic effects are dependent on the band gap energy E_g . For quantum well materials, $\text{In}_y\text{Ga}_{1-y}\text{As}_x\text{P}_{1-x}$ E_g is found as a function of the arsenic mole fraction x (19) [16]. Lattice matching of the $\text{In}_y\text{Ga}_{1-y}\text{As}_x\text{P}_{1-x}/\text{InP}$ system is obtained by the selection of the indium mole fraction y in accordance with (20) [13].

$$E_g(x, T) = 1.35 - 0.72x + 0.12x^2 + (T - 300)(3.18 - 0.41x + 0.61x^2)10^{-4}, \quad (19)$$

where T is the absolute temperature.

$$y(x) = \frac{16.17x - 33.41}{x - 33.41}. \quad (20)$$

The difference between the output and input light wave phases $\Delta\varphi$ for a single section of the internal electrodes is found from Δn_{WG} using (21).

$$\Delta\varphi = \frac{2\pi \cdot P \cdot FF}{\lambda_0} \Delta n_{WG}, \quad (21)$$

where λ_0 is the wavelength of light in vacuum.

The intensity of the light in the output I_{out} of the EOM depends on $\Delta\varphi$ and intensities of the light in the outputs of the EOM arms I_1 and I_2 . The I_{out} can be calculated using (22) [17].

$$I_{out} = I_1 + I_2 + 2\sqrt{I_1 I_2} \cdot \cos(2\Delta\varphi). \quad (22)$$

This equation describes the result of light interference, which occurs at the point of conjunction of the EOM arms. Function (22) is continuous, which provides either analog or digital optical signal modulation.

2.2.3. Optical Loss

Propagation of the optical wave in the waveguide media is accompanied by attenuation of this wave. Power loss of the optical signal occurs due to various mechanisms, both in the volume of the material and on the surface of the waveguide structure. In the method proposed in this paper,

we considered only losses associated with three mechanisms in the volume of an ideal semiconductor. The total attenuation constant α_{total} of arbitrary semiconductor materials can be expressed as (23).

$$\alpha_{total} = \alpha_{ib} + \alpha_E + \alpha_{fk}, \quad (23)$$

where α_{ib} is the attenuation associated with free charge carriers [18], see (24); α_E is the attenuation associated with the external electric field when the band gap energy is much more than the photon energy [19], see (25); and α_{fk} is the optical loss associated with the Franz-Keldysh effect [20], see (26).

$$\alpha_{ib} = \frac{N_c q^3 \lambda_0^2}{4\pi^2 n m_{eff}^2 c^3 \mu \epsilon_0}, \quad (24)$$

where N_c is the free charge carrier concentration, q is the electron charge, n is the media refractive index, m_{eff} is the charge carrier effective mass, and μ is the charge carrier mobility.

$$\alpha_E = A \frac{\lambda_0 E}{(E_g - E_p)} 10^{-\frac{(B(E_g - E_p))^{\frac{3}{2}}}{E}}, \quad (25)$$

where A and B are the electrical strength parameters for the TE and TM polarizations, E is the electric field applied to the media, λ_0 is the wavelength of the light in the vacuum, E_g is the band gap energy, and E_p is the photon energy.

$$\alpha_{fk} = \frac{B\pi}{nc\omega_p} \left\{ \mu_{elh}^{\frac{3}{2}} \left(1 + \frac{m_0}{m_{hh}}\right) \theta_1^{\frac{1}{2}} \left[\left| Ai' \left(\frac{\omega_g - \omega_p}{\theta_1} \right) \right|^2 - x_1 Ai^2 \left(\frac{\omega_g - \omega_p}{\theta_1} \right) \right] + \mu_{elh}^{\frac{3}{2}} \left(1 + \frac{m_0}{m_{lh}}\right) \theta_2^{\frac{1}{2}} \left[\left| Ai' \left(\frac{\omega_g - \omega_p}{\theta_2} \right) \right|^2 - x_2 Ai^2 \left(\frac{\omega_g - \omega_p}{\theta_2} \right) \right] \right\}, \quad (26)$$

where B is the constant that accounts for the material parameters, the matrix elements between the periodic parts of the Bloch states at the band edges, and the fundamental constants; ω_g is the angular frequency of the band gap; ω_p is the angular frequency of the optical radiation; μ_{elh} and μ_{elh} are the heavy and light electron effective masses in the direction of the electric field; m_0 is the electron mass; m_{hh} and m_{lh} are the heavy and light hole effective masses; θ_i is the function of the reduced effective mass of the electron and heavy or light holes and the electric field; and Ai and Ai' are the Airy function and its derivative.

The model of total optical loss described in this subsection can be modified by introducing additional models of loss mechanisms. For instance, models that take into account the technological features of the manufacturing process (for example, waveguide wall roughness) can be included.

3. Target EOM Parameter Calculation Algorithm

In this section, we consider the target EOM parameters and their calculation algorithm. Although the EOM can be characterized by more than ten parameters, we only considered the following four parameters, which are of primary importance for the performance and cost of the device:

Active length of the EOM arm, defined as the total length of all internal sections l_{arm} ;

Minimal optical loss L_{min} , defined as the ratio of optical power in the output to the optical power in the input in the open EOM state;

Maximal difference in the values of L_{min} in the optical operating wavelength range ΔL_{min} ;

Extinction ratio r_e , defined as the ratio of the optical power in the output in the open EOM state to the optical power in the output in the closed EOM state.

To calculate the values of the target parameters, we took a set of input data. The first group of the input parameters represents the result of the preliminary calculations or measurements and corresponds to the particular design of the TWE. These parameters ensure compliance with the

conditions for matching the optical and electric waves and the value of the characteristic impedance of the microwave transmission line. The second group comprises the variable parameters. It is assumed that the values of these parameters are changed within the specified limits during the calculation.

The input parameter set consists of the following:

1. Maximal frequency of EO conversion f_{3dBEO} . This frequency is used as the reference requirement for the calculation of the two TWE parameters that are used directly in the algorithm described below. The first is the TWE internal electrode period P ; the optimization of this parameter for a 40 GHz EO conversion frequency is given in [21]. The second is the maximal electrical signal loss in the single TWE section $|S_{21}|_1$. As a rule, $|S_{21}|_1$ corresponds to the maximal frequency of the EO conversion. Choosing maximal loss provides a calculation of the target parameters for the “worst” case. The value of $|S_{21}|_1$ can be obtained via simulation results or as a result of scattering parameter measurements;
2. Part of the internal electrodes’ specific capacitance $C_{\mu pin}$ which is associated with the PIN diode structure with respect to (2)–(4). The case when $C_{\mu pin}$ has a maximal available value is preferable for obtaining the maximal efficiency of the EO conversion. An example of TWE optimization based on this principle is given in [22];
3. Arsenic mole fraction in the $In_yGa_{1-y}As_xP_{1-x}$ quantum well layer (x);
4. Internal electrode fill factor (FF);
5. Optical waveguide width (W);
6. InP barrier layer thickness (d_B);
7. $In_yGa_{1-y}As_xP_{1-x}$ quantum well layer thickness (d_Q);
8. InP n -spacer thickness (d_{iN});
9. Quantity of periods in MQW (N);
10. Bias voltage (U_B);
11. Control voltage amplitude ($U_{C max}$).

The calculation algorithm for each combination of input parameters consists of the steps listed below. With the use of $|S_{21}|_1$, the value of the control voltage decay factor D_e can be found according to (27). The voltage decay factor D_e is used to calculate the control voltage at all of the TWE sections, knowing the voltage of the first section from the electrical input and taking into account the effect of the attenuation of the electric control signal in the direction of wave propagation in the electrodes.

$$D_e = \sqrt{|S_{21}|_1}. \quad (27)$$

Knowing D_e , the control voltage in a particular TWE section $U_{C,i}$ can be calculated using (28).

$$U_{C,i} = D_e \cdot U_{C,i-1}. \quad (28)$$

The electric field strength under the electrodes E_i for each internal electrode section i is calculated using (29).

$$E_i = \frac{U_e + U_b + U_{C,i}}{d_{MQW} + d_{iN} + d_{iP}}, \quad (29)$$

where U_e is the equivalent voltage embedded in the PIN junction.

The MQW thickness d_{MQW} used in (29) is calculated using (30).

$$d_{MQW} = N(d_Q + d_B). \quad (30)$$

InP p -spacer thickness (d_{iP}) is calculated from the other parameters to satisfy condition (5).

During the calculation, three values of U_C in the first TWE section are considered: $U_{C,1} = 0$ V, when there is no control voltage applied, which corresponds to no control signal in the electrical

input; and $U_{C,1} = U_{C \max}/2$ and $U_{C,1} = -U_{C \max}/2$ for the calculation of the maximal phase difference between the EOM arm outputs in the MZI configuration. Dividing $U_{C \max}$ by two takes into account that the whole voltage U_C applied to the external electrodes is split in half between the two PIN diode structures connected in a serial manner. Furthermore, the corresponding values of the electric field are calculated: $E_{0,i} = E_i(U_{C,1} = 0 \text{ V})$, $E_{H,i} = E_i(U_{C,1} = \frac{U_{\max}}{2})$, and $E_{L,i} = E_i(U_{C,1} = -U_{\max}/2)$.

The distribution of the electric field along the EOM arms founded in the previous step provides the calculation of the total phase shift $\Delta\varphi$ of two optical signals at the point of waveguide coupling (31). The minimal quantity of the internal electrode sections k is selected to satisfy the condition $|\Delta\varphi| \geq \pi$.

$$\Delta\varphi = \frac{2\pi \cdot P \cdot FF}{\lambda} \sum_{i=1}^k \{[\Delta n_{\text{WG}}(E_{H,i}) - \Delta n_{\text{WG}}(E_{L,i})] \cdot \Gamma_{\text{MQW}}\}, \quad (31)$$

where Γ_{MQW} is the optical fill factor corresponding to the whole MQW stack, including all quantum well and barrier layers.

The quantity of sections is calculated at the maximal wavelength. This condition guarantees the phase shift $|\Delta\varphi| \geq \pi$ for the whole optical wavelength range, because at longer wavelengths, the EO conversion efficiency is lower.

At this stage, the first target parameter l_{arm} is calculated using (32).

$$l_{\text{arm}} = P \cdot k. \quad (32)$$

The calculation of the second target parameter L_{min} is performed using (33).

$$L_{\text{min}} = 10 \lg \left[e^{-(A_{\text{act}} + A_{\text{pas}})} \right], \quad (33)$$

where A_{act} is the total loss in the active part of the optical waveguide, see (34); and A_{pas} is the total loss in the passive part of the optical waveguide, see (35).

$$A_{\text{act}} = \sum_{i=1}^k \alpha_{\text{act},i}(E_i) \cdot P \cdot FF, \quad (34)$$

where $\alpha_{\text{act},i}(E_i)$ is the attenuation constant in the waveguide covered by internal electrodes, see (36).

$$A_{\text{pas}} = k \cdot \alpha_{\text{pas}} \cdot P \cdot (1 - FF), \quad (35)$$

where α_{pas} is the attenuation constant in the waveguide not covered by internal electrodes, see (37).

$$\alpha_{\text{act},i} = \Gamma_{\text{QW}} \cdot \alpha_{\text{QW},i} + \Gamma_{\text{B}} \cdot \alpha_{\text{B},i} + \Gamma_{\text{p}} \cdot \alpha_{\text{p},i} + \Gamma_{\text{n}} \cdot \alpha_{\text{n},i}, \quad (36)$$

where Γ_{QW} , Γ_{B} , Γ_{p} , and Γ_{n} are the optical fill factors for the quantum well layers, the barrier layers and spacers, the p^+ InP layer, and the n^+ InP layer, respectively; and α_{QW} , α_{B} , α_{p} , and α_{n} are the attenuation constants for the InGaAsP layers, the undoped InP layers, the p^+ InP layer, and the n^+ InP layer, respectively.

$$\alpha_{\text{pas}} = \Gamma_{\text{QW}} \cdot \alpha_{\text{QW}} + \Gamma_{\text{B}} \cdot \alpha_{\text{B}} + \Gamma_{\text{n}} \cdot \alpha_{\text{n}}. \quad (37)$$

The Γ_{MQW} in (36) and (37) represents the sum of the optical fill factors of all of the InGaAsP layers included in the MQW. Similarly, the Γ_{B} represents the sum of the optical fill factors of all of the undoped InP layers in the heterostructure stack (i.e., MQW barrier layers, p -spacer, and n -spacer). This assumption was made because layers made of the same materials have equal optical properties and are influenced by the same electric field.

The value of the third target parameter ΔL_{min} is obtained by calculation of L_{min} for the limits of the operating wavelength range (38), because the function $L_{\text{min}}(\lambda)$ is represented by a monotonic dependence.

$$\Delta L_{\text{min}} = |L_{\text{min}}(\lambda_{\text{min}}) - L_{\text{min}}(\lambda_{\text{max}})|. \quad (38)$$

The value of the fourth target parameter r_e is calculated using (39):

$$r_e = L_{min0} - 10 \lg \left[\frac{T_+}{2} + \frac{T_-}{2} - \sqrt{T_+ \cdot T_-} \right] \quad (39)$$

where L_{min0} is the optical loss for $U_{c,1} = 0$; $T_+ = e^{-(A_{act}(U_{c,1}=U_{max}/2)+A_{pas})}$ is the portion of the optical signal passed through the first EOM arm when a positive control voltage is applied; and $T_- = e^{-(A_{act}(U_{c,1}=-U_{max}/2)+A_{pas})}$ is the portion of the optical signal passed through the second EOM arm when a negative control voltage is applied.

The part of Equation (39) after the “−” sign represents the minimal optical power in the output of the EOM that can be obtained. This follows from (22) under the condition of $\Delta\varphi = \pi$.

4. EOM Optimization Example

In this section, we demonstrate how the described method can be used for 1530–1560 nm EOM optimization.

4.1. Input Parameter Limits

In order to perform the calculations, the values or ranges of all of the input parameters introduced in Section 3 should be stated. In this subsection, we indicate the values of the input parameters and briefly substantiate the reasons for their selection.

The maximal frequency of the EO conversion $f_{3dB_{EO}}$ was chosen to be 40 GHz. The values of $P = 150 \mu\text{m}$ [21], $C_{\mu pin} = 192 \text{ pF/m}$ [22], and $|S_{21}|_1 = 0.923$ were obtained for this particular TWE design and the specified value of $f_{3dB_{EO}}$.

The arsenic mole fraction x varied from 0.73 to 0.77 in 0.01 steps. For $x < 0.73$, the control voltage has a weak dependence on the refractive index, and the required phase shift is difficult to obtain. For $x > 0.77$, the optical loss increases greatly due to exciton absorption and band-to-band transitions.

The electrical fill factor FF varied from 0.7 to 0.85 in 0.05 steps. The preliminary calculations showed that $FF < 0.7$ is impractical due to the increase in the length and optical loss. For $FF > 0.85$, the waveguide PIN diode structure must have a lower specific capacitance value. This means that the waveguide width W should be decreased or the value of the sum $(d_{MQW} + d_{iN} + d_{iP})$ should be increased, which leads to an increase in the optical loss or a decrease in the EO conversion efficiency.

The optical waveguide width W varied from 1600 to 2000 nm in 100 nm steps. Lower values were limited by technological constraints, while the upper value was limited to provide a relatively low waveguide specific capacitance.

The barrier layer thickness d_B varied from 6 to 10 nm in 2 nm steps. For $d_B < 6 \text{ nm}$, the resonant tunneling effect (Wannier-Stark effect) takes place and leads to an increase in the optical loss [23]. An increase in d_B by more than 10 nm leads to a decrease in the optical fill factor of the quantum well layers and, hence, a decrease in the EO conversion efficiency.

The quantum well thickness d_Q varied from 14 to 22 nm in 2 nm steps. Values of $d_Q < 12\text{--}14 \text{ nm}$ are impractical because they correspond to a low MQW optical fill factor and EO conversion efficiency. Values of $d_Q > 22 \text{ nm}$ may lead to an increase in the mechanical stress in MQW and to defects in the density in a semiconductor structure [24].

The quantity of the quantum wells N varied from 12 to 22 in steps of 2. Values of $N < 14$ correspond to a low quantum well optical fill factor and a low EO conversion efficiency. The upper value of N was limited to 20–25 due to the technological constraints. The available semiconductor wafer vendor cannot guarantee surface conditions during the growth of such an InGaAsP/InP heterostructure composition.

The thickness of the n -spacer d_{iN} was set to a constant value of 50 nm. Although this parameter can be varied as well, the specified value was found to be optimal. Using lower values of d_{iN} leads to an increase in the optical signal loss in the n^+ -InP contact layer. Using higher values of d_{iN} leads to a decrease in the thickness of MQW or d_{iP} . Both cases lead to the degradation of the EO conversion efficiency or to an increase in the optical loss in the p^+ -InP layer.

The values of the bias voltage U_B were chosen to be 2 and 3 V. PIN diodes incorporated in waveguide structures perform at reverse bias. The preliminary calculations showed that such U_B values provide the most linear dependence $\Delta n_{WG}(U_B)$, which is preferable for analog modulation. A U_B range from 2 to 3 V corresponds to both low optical loss and high EO conversion efficiency.

The control voltage $U_{C\ max}$ was limited to a value of 2 V. This provides the ability to use the radio frequency driver with an output power not exceeding 20 mW in the EOM electrical input.

4.2. Calculation Results and Data Analysis

The target EOM parameters were calculated for each combination of the input parameters using the algorithm described in Section 3. A computer program was developed to perform this task because, in this case, we dealt with more than 13,000 combinations of input parameters.

The data obtained as a result of the calculation were preliminarily filtered using the limits for the target parameters listed in Table 1. In this step, all of the combinations were filtered by only one target parameter, so the results could include combinations that were outside of the limits corresponding to the other target parameters. Thereby, four sets of combinations were created: one set for each target parameter.

Table 1. Target parameter limits for the calculated data filtering.

Target Parameter Limits	Value	
	$U_B = 2\ \text{V}$	$U_B = 3\ \text{V}$
l_{arm} upper limit, mm	2.25	1.95
L_{min} upper limit, dB	0.5	0.6
ΔL_{min} upper limit, dB	0.2	0.54
r_e lower limit, dB	38	33

The data are presented graphically in Figures 4 and 5 for $U_B = 2\ \text{V}$ and $U_B = 3\ \text{V}$, respectively. Each graph in Figures 4 and 5 represents a set of input parameter combinations forming a “cloud” that satisfies a given value of a particular target parameter.

It can be seen from Figures 4 and 5 that it is impossible to find a combination of all of the six input parameters that belongs to all four “clouds” at a given U_B . However, some of the values of the input parameters W , d_B , d_Q , and N (as well as FF for $U_B = 3\ \text{V}$) may correspond to near-optimal values of all of the target parameters simultaneously. This approach allows detecting the input parameters that are the most critical for the EOM design: x and FF . The values of these input parameters should be chosen separately to tune the performance of the EOM.

It should be noted that the “clouds” in Figures 4 and 5 depend on the limits used during the preliminary data filtering. One may face the situation when more than two parameters are detected as critical. In this case, it is recommended to lower the limits of the filtering so as to obtain only two or three critical parameters.

A comparison of the results for $U_B = 2\ \text{V}$ and $U_B = 3\ \text{V}$ shows that although the general picture stays approximately the same, the variation in U_B from 2 to 3 V has an influence on the absolute values of the target parameters. Analysis of results with different U_B values allows selecting the optimal bias voltage at the stage of critical parameter selection. Since the critical parameters are known, optimization of the EOM is performed as follows. Constant values of the input parameters $W = 1.7\ \mu\text{m}$, $d_B = 8\ \text{nm}$, $d_Q = 20\ \text{nm}$, and $N = 18$ located inside all four “clouds” simultaneously at a particular U_B were chosen (except in Figure 5b, where the value $W = 1.7\ \mu\text{m}$ was close to the “cloud” but did not belong to it). In the next step, the dependences of the target parameters on x at different FF were plotted for $U_B = 2\ \text{V}$ and $U_B = 3\ \text{V}$ (see Figure 6).

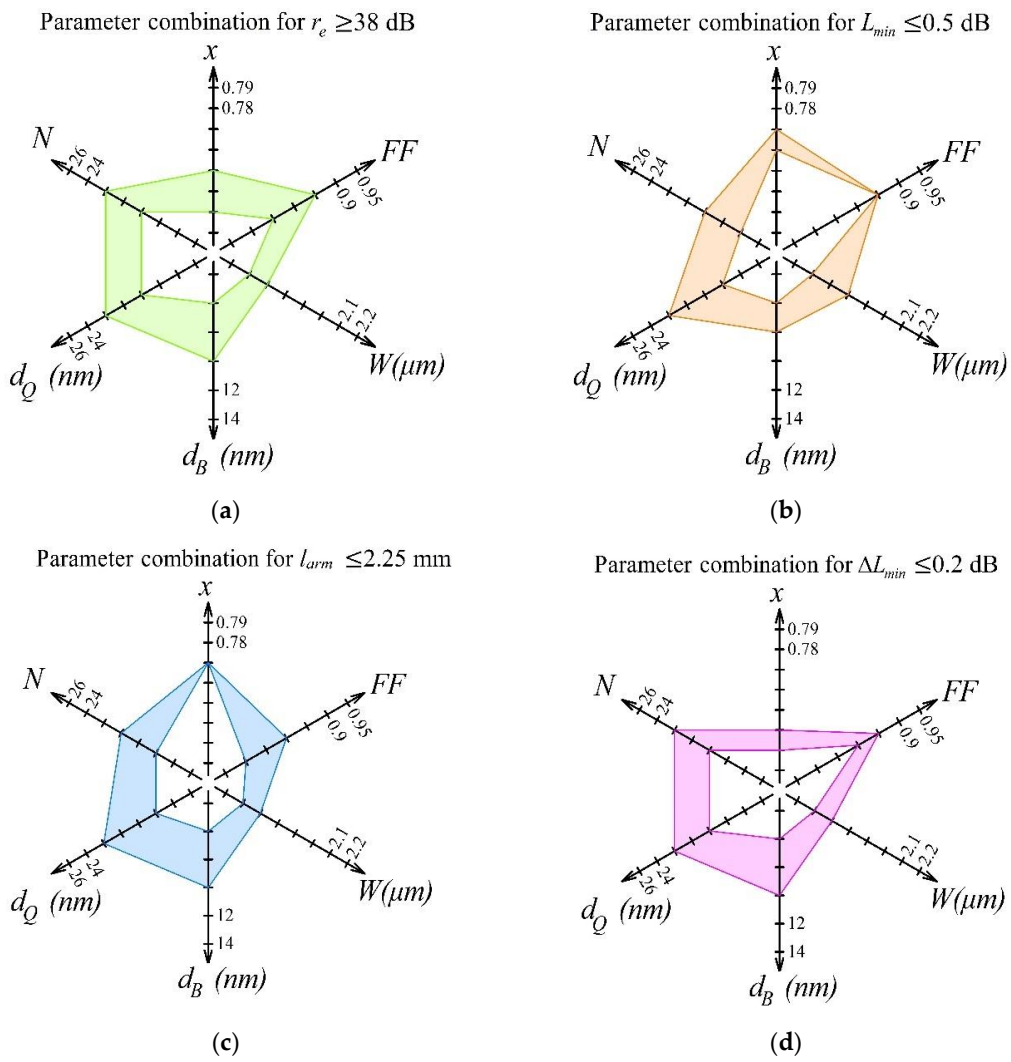


Figure 4. Sets of input parameter combinations at $U_B = 2$ V, satisfying the limits for: (a) extinction ratio (r_e); (b) minimal optical loss (L_{min}); (c) active length of the EOM arm (l_{arm}); and (d) maximal difference of optical loss in the operating wavelength range (ΔL_{min}).

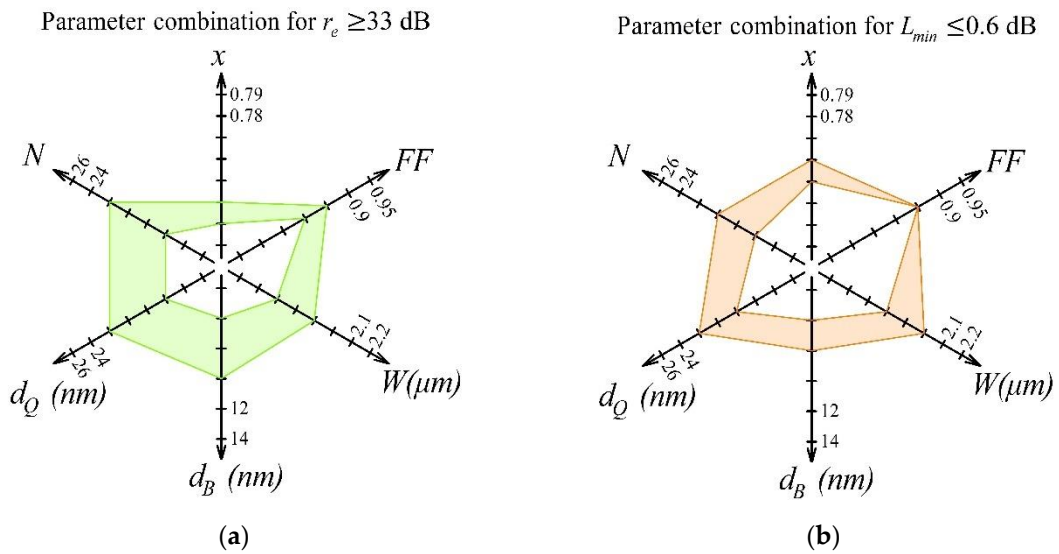


Figure 5. Cont.

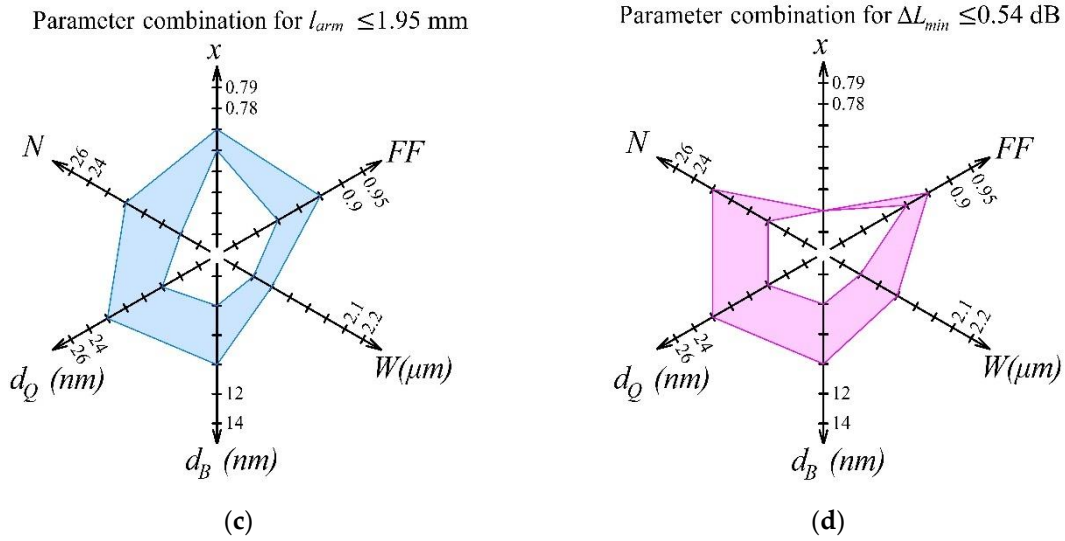


Figure 5. Sets of input parameter combinations at $U_B = 3$ V, satisfying the limits for: (a) extinction ratio (r_e); (b) minimal optical loss (L_{min}); (c) active length of the EOM arm (l_{arm}); (d) and maximal difference of optical loss in the operating wavelength range (ΔL_{min}).

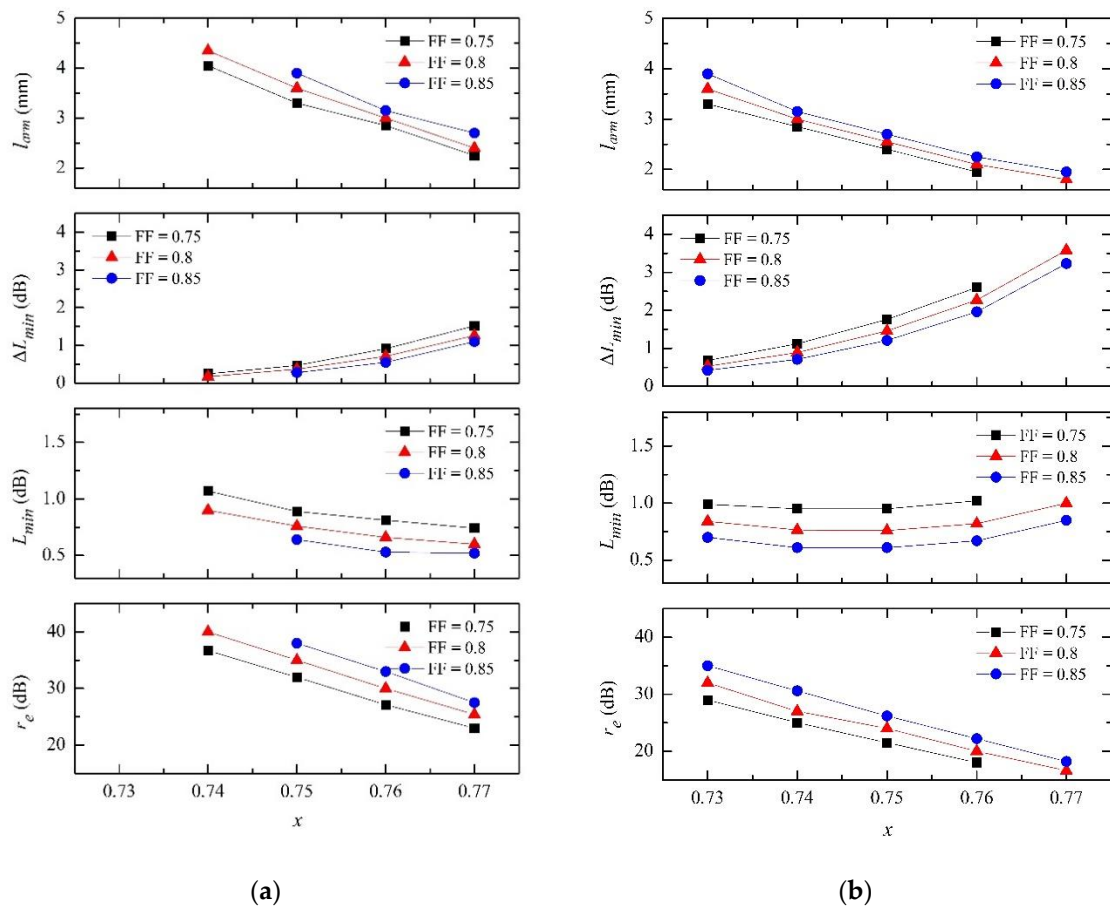


Figure 6. EOM target parameters versus arsenic mole fraction (x) and electrical fill factor (FF) at: (a) bias voltage $U_B = 2$ V; and (b) bias voltage $U_B = 3$ V.

The subsequent selection of U_B , x , and FF was performed as follows. A comparison of Figure 6a,b shows that a lower value of l_{arm} can be obtained at $U_B = 3$ V, which corresponds to a higher EO conversion efficiency. However, a higher electric field in the waveguide structure caused sufficient

degradation of the other target parameters, especially the extinction ratio. Due to this fact, $U_B = 2$ V was chosen as the preferable value, and further analysis was performed for this bias voltage.

As can be seen from Figure 6a, a lower arsenic mole fraction x corresponds to better r_e and ΔL_{min} values. However, the lowest x values (0.74 and 0.75) are not optimal due to the following reasons. First, using low values of x corresponds to a greater area chip and a higher device cost, which are associated with higher l_{arm} values. Second, higher l_{arm} values cause a higher optical loss, which includes the calculated part (L_{min}), as well as technology-dependent optical loss associated mainly with the waveguide wall roughness. This loss is proportional to the waveguide length and may exceed the value of L_{min} . The highest value of x (0.77) is impractical because it corresponds to poor r_e and ΔL_{min} . Finally, the values of $x = 0.76$ and $FF = 0.85$ were chosen in this EOM optimization example to obtain the optimal balance of the target parameters.

The resulting EOM parameters are summarized in Table 2 and are given together with the parameters implemented in some published devices.

Table 2. The target and design parameters of the EOM in comparison to published devices.

Parameter	Unit	Klein [8]	Chen [12]	Juodawlkis [25]	This Work
λ_{min}	nm	1535	n/d ¹	n/d	1530
λ_{max}	nm	1565	n/d ¹	1560	1560
$f_{3dB_{eo}}$	GHz	45	45	n/d	40
L_{min}	dB	0.6–0.7	n/d	2.1	0.54
ΔL_{min}	dB	n/d	n/d	n/d	0.56
r_e	dB	24	n/d	20	32.8
l_{arm}	mm	3	4	3	3.15
U_B	V	4	2.8	5	2
$U_{C\ max}$	V	2	2.6	1	2
P	μ m	<200	125	n/d	150
$C_{\mu\ pin}$	pF/m	n/d	n/d	n/d	192
$ S_{21} _1$	-	n/d	n/d	n/d	0.923
FF	-	0.8	0.5	n/d	0.85
x	-	0.76	n/d	0.77	0.76
y	-	n/d	n/d	n/d	0.65
W	μ m	2	n/d	3	1.7
d_B	nm	8	n/d	8	8
d_Q	nm	12	n/d	12	20
N	-	n/d	20	30	18
d_{iN}	nm	n/d	n/d	50–100	50
d_{iP}	nm	n/d	n/d	300	175
$d_{iN} + d_{iP} + d_{MQW}$	nm	700–800	900	950–1000	729

n/d, no data found. ¹ Designed for 1550 nm wavelength operation.

Analysis of Table 2 highlights some general findings related to the EOM design considered in this work.

The arsenic mole fraction $x = 0.76$ seems to be optimal. In the work of [25], the authors used $x = 0.77$. It can be supposed that the latter could be the reason for the higher value of L_{min} and lower value of r_e in comparison with devices in which $x = 0.76$ is used. In addition, using of $x = 0.77$ and high U_B could allow obtaining a low value of $U_{C\ max} = 1$ V with the short EOM arm [25].

The electrical fill factor FF found in this work as optimal is close to the value implemented in [8]. Comparing the product $FF \times W$ with the data reported in [8] with the same product obtained in this work, we can make the conclusion that these products are close to each other (1.60 and 1.45 μ m, respectively).

The parameters of the MQW optimized in this work are quite close to such parameters of published devices. A barrier layer thickness d_B of 8 nm was chosen as the optimal value for all devices in Table 2 (where data are presented). A quantum well layer thickness d_Q of 12 nm and a quantity of quantum

well layers N in the range of 20–30 were used in the published devices. In this work, we found that it was more optimal to use a higher d_Q together with a lower N if possible. It is notable that compared to the work of [25], the same product $N \times d_Q$ was obtained in this work (360 nm). This corresponds to a similar optimal Γ_{MQW} value found for both cases.

The thickness of the intrinsic region ($d_{iN} + d_{iP} + d_{MQW}$) obtained as a result of this optimization in this work was close to the optimal value implemented in [12] and especially in [8].

The value of the bias voltage U_B chosen in this work was lower than that for the published devices listed in Table 2. We suppose that this mismatch was caused by the method of optimization used in this work. During the optimization, we used ΔL_{min} and r_e as target parameters. Since the value of the total electric field applied to the PIN diode waveguide structure is critical for the specified parameters, a lower U_B value was preferred. It was shown that higher U_B values may be optimal for the reduced requirements for ΔL_{min} and r_e .

The data presented in Table 2 show that, with the use of the method of calculation presented in this work, we obtained target parameter values and an optimized set of input parameters that generally fit the values of the same parameters of similar devices published in [8,12,25].

5. Conclusions

In this work, a method for EOM optimization was proposed and verified. The calculation algorithm is based on the TWE design primacy and is implemented in such a way that the target parameter values are calculated for all sets of input parameter combinations.

Preliminary data filtering and the proposed multi-parameter data representation allow performing convenient analysis of the calculated results and highlighting the input parameters that are the most critical for the performance of the device.

During the EOM optimization using the presented method, we found that a combination of six sufficient input parameters defined the EOM design and that the bias voltage U_B also affected the performance of the EOM. The sufficient input parameters were the thickness of the quantum well layer d_Q , the thickness of the barrier layer d_B , the arsenic mole fraction x , the quantity of quantum layers N , the electrical fill factor of the TWE FF , and the optical waveguide width W . The presented method allows detecting the parameters—herein, x and FF —that are critical for the performance of the EOM.

Author Contributions: Conceptualization, M.S. and V.A.; methodology, I.Y.; software, M.S.; validation, P.T.; formal analysis, M.S.; investigation, M.S.; resources, Y.Z.; data curation, V.A.; writing—original draft preparation, M.S.; writing—review and editing, I.Y.; visualization, Y.Z.; supervision, V.A.; project administration, P.T. All authors have read and agreed to the published version of the manuscript.

Funding: The work was carried out with financial support from the Ministry of Science and Higher Education of the Russian Federation (Project name: Theoretical and experimental studies of ultra-wideband optoelectronic devices of fiber-optic information systems and microwave photonics based on photonic integrated circuits own development; Agreement No. 075-03-2020-237/1 from 05 March 2020; project number FEWM-2020-0040). The experimental results were obtained by the team from the Integrated Optics and Microwave Photonics Laboratory of the Tomsk State University of Control Systems and Radioelectronics using the equipment of the “Impulse” center of collective usage (registration number 200568).

Conflicts of Interest: The authors declare no conflict of interest.

References

1. Mitchel, P.; Longone, R.; Janssen, A.; Garrett, B.; Luo, J.K. Le Evaluation of an InP Mach-Zehnder modulator for high speed optical network system architectures and emerging photonically integrated optical modules. *J. Optoelectron. Adv. Mater.* **2010**, *12*, 965–974.
2. Sun, J.; Timurdogan, E.; Yaacobi, A.; Su, Z.; Hosseini, E.; Cole, D.B.; Watts, M.R. Large-Scale Silicon Photonic Circuits for Optical Phased Arrays. *J. Sel. Top. Quantum Electron.* **2014**, *20*. [[CrossRef](#)]

3. Qing, T.; Xue, M.; Huang, M.; Pan, S. Measurement of optical magnitude response based on double-sideband modulation. *Opt. Lett.* **2014**, *39*, 6174–6176. [[CrossRef](#)]
4. Porte, H.; Kernec, A.; Quesada, L.P.; Esquivias, I.; Brahimi, H.; Gonzalez, J.B.; Mottet, A.; Sotom, M. Optimization and evaluation in space conditions of multi-GHz optical modulators. In Proceedings of the International Conference on Space Optics (ICSO 2014), Tenerife, Canary Islands, Spain, 7–10 October 2014.
5. Zhang, X.; Lee, B.; Lin, C.; Wang, A.X.; Hosseini, A.; Chen, R.T. Highly Linear Broadband Optical Modulator Based on Electro-Optic Polymer. *IEEE Photonics J.* **2012**, *4*, 2214–2228. [[CrossRef](#)]
6. Chen, R.T.; Shih, R.; Robinson, D.; Jansson, T. Single-Mode optically activated phase modulator on GaAs/GaAlAs compound semiconductor rib waveguides. *J. Appl. Phys.* **1993**, *74*, 5964–5971. [[CrossRef](#)]
7. Baier, M.; Grote, N.; Moehrl, M.; Sigmund, A.; Soares, F.M.; Theurer, M.; Troppenz, U. Integrated transmitter devices on InP exploiting electro-absorption modulation. *Photonix* **2020**, *1*, 4. [[CrossRef](#)]
8. Klein, H. Integrated InP Mach-Zehnder Modulators for 100 Gbit/s Ethernet Applications Using QPSK Modulation. Ph.D. Thesis, Berlin Institute of Technology, Berlin, Germany, 2010.
9. Wang, H.-T.; Zhou, D.-B.; Zhang, R.-K.; Lu, D.; Zhao, L.-J.; Zhu, H.-L.; Wang, W.; Ji, C. Optimization of 1.3- μm InGaAsP/InP Electro-Absorption Modulator. *Chin. Phys. Lett.* **2015**, *32*, 084203. [[CrossRef](#)]
10. Stanley, A.I.; Singh, G.; Eke, J.; Tsuda, H. Mach-Zehnder Interferometer: A review of a perfect all optical switching structure. In Proceedings of the International Conference on Recent Cognizance in Wireless Communication & Image Processing (ICRCWIP 2015), New Delhi, India, 16 January 2016; pp. 415–426.
11. Kim, S.; Lee, C.; Song, M.; Kwak, M.H. Design and characterization for travelling wave electrodes of high-Speed Mach-Zehnder electro-Optic modulator on an n-Doped InP substrate. *Microw. Opt. Technol. Lett.* **2018**, *60*, 1558–1562. [[CrossRef](#)]
12. Chen, H. Development of an 80 Gbit/s InP-based Mach-Zehnder Modulator. Ph.D. Thesis, Berlin Institute of Technology, Berlin, Germany, 2007.
13. Van de Hulsbeek, A.J.G.M. Design, Fabrication and Characterization of a Mach-Zehnder Interferometric Switch within the POLarization Based Integration Scheme (POLIS). Master's Thesis, Eindhoven University of Technology, Eindhoven, The Netherlands, 2006.
14. Adachi, S.; Oe, K. Linear electro-optic effects in zincblende-type semiconductors: Key properties of InGaAsP relevant to device design. *J. Appl. Phys.* **1984**, *56*, 74–80. [[CrossRef](#)]
15. Maat, D.H.P. InP-Based Integrated MZI Switches for Optical Communication. Ph.D. Thesis, Delft University of Technology, Delft, The Netherlands, 2001.
16. Weber, J.P. Optimization of the carrier-induced effective index change in InGaAsP waveguides-application to tunable Bragg filters. *IEEE J. Quantum Electron.* **1994**, *30*, 1801–1815. [[CrossRef](#)]
17. Sharma, U.; Wei, X. Fiber Optic Interferometric Devices. In *Fiber Optic Sensing and Imaging*; Kang, J.U., Ed.; Springer: New York, NY, USA, 2013; pp. 29–53.
18. Hunsperger, R.G. *Integrated Optics: Theory and Technology*; Springer Series in Optical Sciences; Springer: Berlin, Germany, 1982.
19. Callaway, J. Optical Absorption in an Electric Field. *Phys. Rev.* **1963**, *130*, 549–553. [[CrossRef](#)]
20. Bennet, B.R.; Soref, R.A. Electrorefraction and Electroabsorption in InP, GaAs, GaSb, Ids, and InSb. *IEEE J. Quantum Electron.* **1987**, *23*, 2159–2166. [[CrossRef](#)]
21. Yunusov, I.V.; Arykov, V.S.; Stepanenko, M.V.; Troyan, P.E. Optimization of RF Electrodes for Electro-Optic Modulator Based on Quantum-Confined Stark Effect. In Proceedings of the 20th International Conference of Young Specialists on Micro/Nanotechnologies and Electron Devices (EDM 2019), Erlagol, Russia, 29 June–3 July 2019; pp. 291–295.
22. Stepanenko, M.V.; Yunusov, I.V.; Kulinich, I.V. Optimization of RF electrodes for electro-optic modulator based on quantum-confined Stark effect. *J. Phys. Conf. Ser.* **2019**, *1145*, 012028. [[CrossRef](#)]
23. Soucail, B.; Dupuis, N.; Ferreira, R.; Voisin, P.; Roth, A.P.; Morris, D.; Gibb, K.; Lacelle, C. Electron minibands and Wannier-Stark quantization in an In_{0.15}Ga_{0.85}As-GaAs strained-layer superlattice. *Phys. Rev. B* **1990**, *41*, 8568–8571. [[CrossRef](#)] [[PubMed](#)]
24. Evans, J.D. Effects of Intentionally Introduced Mismatch Strain on the Operating Characteristics and Temperature Performance of InGaAsP/InP Long Wavelength Semiconductor Lasers. Ph.D. Thesis, McMaster University, Hamilton, ON, Canada, 1993.

25. Juodawlkis, P.W.; O'Donnell, F.J.; Bailey, R.J.; Plant, J.J.; Ray, K.G.; Oakley, D.C.; Napoleone, A.; Watts, M.R.; Betts, G.E. InGaAsP/InP quantum-well electrorefractive modulators with sub-volt $V\pi$. In Proceedings of the SPIE, Enabling Photonic Technologies for Aerospace Applications VI, Orlando, FL, USA, 12–16 April 2004; Volume 5435, pp. 53–63.

Publisher's Note: MDPI stays neutral with regard to jurisdictional claims in published maps and institutional affiliations.



© 2020 by the authors. Licensee MDPI, Basel, Switzerland. This article is an open access article distributed under the terms and conditions of the Creative Commons Attribution (CC BY) license (<http://creativecommons.org/licenses/by/4.0/>).